Journal of Nuclear Materials 548 (2021) 152840

Contents lists available at ScienceDirect

Journal of Nuclear Materials

journal homepage: www.elsevier.com/locate/jnucmat

Modeling fission product diffusion in TRISO fuel particles with BISON

Jason D. Hales*, Wen Jiang, Aysenur Toptan, Kyle A. Gamble

Idaho National Laboratory, Computational Mechanics & Materials Department, PO Box 1625, Idaho Falls, ID 83415, United States

ARTICLE INFO

Article history:
Received 14 December 2020
Revised 18 January 2021
Accepted 20 January 2021
Available online 11 February 2021

Keywords:
TRISO fuel
Verification
Validation
AGR-1
BISON

ABSTRACT

The diffusion of fission products in intact TRISO particles depends on particle geometry, fission product source rates, time, temperature, and temperature-dependent diffusion coefficients. Simulating this diffusion process requires models for source rates and diffusion coefficients, plus a computation of the temperature field if not prescribed. In addition, the simulation quality depends on the discretization of the geometry, appropriate time stepping, and the accuracy of the solution method.

In this paper, we explore the simulation of fission product diffusion in TRISO fuel particles using the finite element method via the fuel performance code BISON. Recent material model development has occurred in BISON for each material present in tri-structural isotropic (TRISO) fuel particles: the buffer, inner pyrolytic carbon, silicon carbide, and outer pyrolytic carbon layers, as well as the fuel kernel. Also, new mesh generation and fission product release fraction capabilities have been added.

Diffusion capabilities are shown to converge to the correct solution via formal verification tests. A large number of code benchmarking problems are also given, with good results, showing that BISON's computed release fractions closely match those of other software tools. Finally, a significant validation effort is detailed in which fission product release, measured as part of the AGR-1 capsule experiments, is compared to BISON outputs. BISON outputs compare favorably to the experimental data and to PARFUME results.

1. Introduction

The evaluation of TRISO fuel using the BISON fuel performance code was the subject of [1]. That paper reviewed the basic structure of TRISO fuel and discussed some of its history, including various efforts to simulate TRISO behavior with computer models. It also discussed several verification and benchmarking problems. Much of that discussion relied upon a Coordinated Research Program (CRP-6) through the International Atomic Energy Agency (IAEA) [2]. A handful of simple problems with analytic solutions, along with a few more complicated problems without analytic solutions but with computed solutions supplied by Coordinated Research Program (CRP-6) participants, were used to demonstrate the correctness of BISON's predictions.

AGR-1 was the first in a series of irradiation tests on TRISO particle fuel sponsored by the U.S. Department of Energy (DOE)'s Advanced Gas Reactor program. One of the objectives was to examine the release of silver, cesium, and strontium. The experiment included a total of 72 compacts, arranged twelve to a capsule, with six capsules total. post-irradiation examination (PIE) on these compacts measured fission product release and identified specific compacts with failed particles and the number of failed particles. In addition, irradiation conditions, including power level and compact-average temperature, are available for each day of irradiation. This data has been used to evaluate the quality of computationally predicted fission product release [3].

The focus of the current work is to explore more fully the diffusion of fission products in TRISO fuel. To do so, we first review the fundamental equations governing mass diffusion and discuss specific models implemented to model that behavior (Section 2). Next, we discuss a mathematically rigorous verification of those equations (Section 3). This is followed by a discussion of CRP-6 benchmark cases where we first revisit the results from [1] and then show results from remaining cases (Section 4). Following that discussion, we give validation results wherein we compare solutions computed by BISON to AGR-1 data and results computed by PARFUME [4] (Section 5).

2. Equations and modeling capabilities

The TRISO capabilities in BISON are based on the three partial differential equations at the center of all fuel performance mod-

* Corresponding author.
E-mail addresses: jason.hales@inl.gov (J.D. Hales), jason.hales@inl.gov (K.A. Gamble).

https://doi.org/10.1016/j.jnucmat.2021.152840
0022-3115/

eling activities: conservation of momentum or static equilibrium (Eq. (1)), energy balance or the heat equation (Eq. (2)), and mass diffusion (Eq. (3)).

Conservation of momentum, or static equilibrium, is prescribed using Cauchy's equation:

$$\nabla \cdot \boldsymbol{\sigma} + \rho \mathbf{f} = 0 \tag{1}$$

where $\boldsymbol{\sigma}$, the Cauchy stress tensor, is a function of displacement, the primary variable. Stress is often a complicated function of temperature and irradiation history. $\mathbf{f}$ is the body force per unit mass (e.g., gravity). This equation is used in the section on fuel performance analysis Section 4.1 but is not active in the other analyses shown here.

The heat equation is:

$$\rho C_p \frac{\partial T}{\partial t} + \nabla \cdot \mathbf{q} - E_f \dot{F} = 0 \tag{2}$$

where T is temperature, the primary unknown; ρ and C_p are density and specific heat; $\mathbf{q}$ is the heat flux; E_f is the energy released per fission; and $\dot{F}$ is the volumetric fission rate.

Fission product species conservation, or mass diffusion, is given by:

$$\frac{\partial C}{\partial t} + \nabla \cdot \mathbf{J} + \lambda C - S = 0 \tag{3}$$

where C is concentration, the primary variable; λ and S are the radioactive decay constant and source rate of a given species; and $\mathbf{J}$ is the mass flux. Radioactive decay is not used in this study.

Details of material models used in these equations are available in [5]. Note that BISON expects inputs in SI units. The code handles any required conversions for material models based on empirical relationships.

Nominally, TRISO fuel is spherically symmetric. Using this symmetry, the governing equations of stress, heat transfer, and fission product transfer may be simplified greatly. This fact is leveraged by tools such as PARFUME (Particle Fuel Model) and enables quick analyses of standard particles. Although TRISO particles fail infrequently, they do fail, and the failures occur in ways that are not spherically symmetric. In order for a code restricted to spherical symmetry to calculate failure information, another tool is needed. In the case of Particle Fuel Model (PARFUME), multidimensional, a (an) calculations from Abaqus [6] are required to give insight into failure behavior [4,7].

In contrast, BISON's inherent ability to model a variety of geometries gives it the potential to model TRISO fuel in all situations, including particles with manufacturing defects. This was highlighted in [1]. In this paper, we focus on mass diffusion in spherically symmetric particles. See [8] for a discussion of TRISO fuel performance and failure analysis using BISON.

2.1. Recent TRISO development in BISON

Mechanical, thermal, and mass diffusion models must be defined for each material in a full fuel performance analysis. Details of these models are available at the BISON website [5]. These models are available in BISON as C++ classes and are invoked through appropriate statements in the input file. Using the interfaces in the code, it is straightforward to add new material models and other modeling capabilities. This allowed the rapid inclusion of new capabilities discussed below. Other models may be added in a similar fashion. In addition, it is often possible to utilize generic material models that allow relatively complex behavior to be described using only input file commands. Mesh generation capabilities, fission product diffusion models, and fission yield models–all essential for diffusion calculations–are highlighted here.

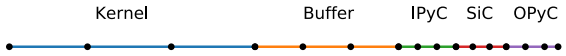

Fig. 1. A simple one-dimensional mesh for a TRISO particle. Each material is represented by three finite elements.

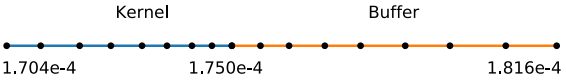

Fig. 2. A close-up view of a portion of a TRISO mesh where the kernel ends and the buffer begins. The mesh becomes more refined toward the interface due to biasing. The coordinates on the figure are for the left-most node, the node at the interface of the kernel and the buffer, and the right-most node.

2.1.1. Mesh generation

Analysis of TRISO fuel particles typically assumes perfect spherical geometry. With that assumption, the domain can be represented by a line of one-dimensional ans. Each material layer in the TRISO fuel particle is represented by a set of ans grouped together and labeled so BISON can apply the appropriate material properties to the different layers. The schematic in Fig. 1 shows elements grouped according to the material they represent and the nodes that define them.

Specialized software is often used to generate an meshes. However, BISON has the ability to generate one- and two-dimentional TRISO meshes internally. To use the one-dimensional capability, three main inputs are required for each of the kernel, buffer, inner pyrolytic carbon (PyC), silicon carbide, and outer PyC materials. These are the thickness (radius, for the kernel), the number of elements for each material, and a meshing bias.

The meshing bias allows elements to be concentrated toward one end of the material. The bias parameter b represents the length of an element based on the length of the element to its left. For example, if $b = 0.8$, the elements will get smaller from left to right, concentrating more elements at the right side of the material. If $b = 1.5$, the elements will grow in size from left to right, with more, smaller elements at the left side of the material. An example of this bias feature is shown in Fig. 2. As can be seen, the ans decrease in size in the kernel portion of the mesh and increase in size in the buffer portion. Biasing the mesh in this way is helpful when there are dramatic changes in diffusivity, as is the case with strontium diffusivity in the kernel and buffer. See Section 5.2 for details. For the AGR-1 validation studies in this work, the mesh consisted of 18, 14, 6, 8, and 6 elements over the fuel, buffer, IPyC, SiC, and OPyC. A bias of 0.8 was applied in the kernel, and a bias of 1.25 was applied in the buffer.

For a failure analysis, two-dimensional and three-dimensional meshes are needed. Simple two-dimensional meshes of TRISO particles can be built by BISON. For example, Fig. 3 shows a two-dimensional mesh of a quarter of a TRISO particle sectioned through its center. This mesh would be used in an axisymmetric analysis.

More complex two- or three-dimensional meshes require specialized software such as CUBIT [9].

2.1.2. Fission product diffusion

Fission product diffusion follows Eq. (3). The mass flux $\mathbf{J}$ is:

$$\mathbf{J} = -D \nabla C \tag{4}$$

where the diffusion coefficient, D (m^2/s), is defined in Arrhenius form as:

$$D = \sum_i D_{0,i} \exp\left(\frac{-Q_i}{RT}\right) \tag{5}$$

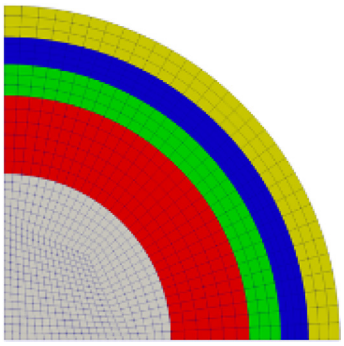

Fig. 3. A two-dimensional mesh of a TRISO particle. This mesh may be created in BISON according to user preferences.

Table 1
Mass diffusion coefficients.

		Kernel (UO_2)	PyC	SiC
Ag	$D_{0,1}$ (m^2/s)	6.7×10^{-9}	5.3×10^{-9}	3.6×10^{-9}
	Q_1 (kJ/mol)	165	154	215
Cs	$D_{0,1}$ (m^2/s)	5.6×10^{-8}	6.3×10^{-8}	5.5×10^{-14}
	Q_1 (kJ/mol)	209	222	125
Sr	$D_{0,1}$ (m^2/s)	2.2×10^{-3}	2.3×10^{-6}	1.2×10^{-9}
	Q_1 (kJ/mol)	488	197	205

where R is the universal gas constant. Typical values of $D_{0,1}$ and Q_1 for silver, cesium, and strontium are given in Table 1 [3]. Additional terms targeting high-temperature behavior are often used. A model where $D_{0,1}$ is a function of the fast neutron fluence is also commonly used [10].

In BISON, other values for $D_{0,i}$ and Q_i may be used by entering those values in the input file. More complicated expressions, including expressions that are functions of other fields, may often be entered directly in the input file.

In BISON, the temperature field used by diffusion models can either be fully prescribed as input or be determined via solving the heat conduction equation. When the temperature is fully described, it may still vary in space and time.

2.1.3. Fission yields

Fission yields, Γ (atoms/fission), for silver, cesium, and strontium are given below.

- For silver:

$$\Gamma_{Ag} = \begin{cases} 1.31625 \times 10^{-3} b^{0.55734} & \text{for } \epsilon < 17.5 \\ 8.24492 \times 10^{-4} b^{0.53853} & \text{for } \epsilon \geq 17.5 \end{cases} \tag{6}$$

  where $b = \max(1.0, Bu)$.
- For cesium:

$$\Gamma_{Cs} = \begin{cases} 0.14 & \text{for } \epsilon < 17.5 \\ 0.16 & \text{for } \epsilon \geq 17.5 \end{cases} \tag{7}$$

- For strontium:

$$\Gamma_{Sr} = \begin{cases} 0.11754 b^{-0.21762} & \text{for } \epsilon < 17.5 \\ 0.11819 b^{-0.15778} & \text{for } \epsilon \geq 17.5 \end{cases} \tag{8}$$

  where $b = \max(0.6, Bu)$. ϵ (%) is the ^{235}U enrichment, and Bu (% FIMA) is the burnup.

Fission yields operate in the source term for the diffusion equation. Like diffusion coefficients, it is straightforward to customize these expressions.

At the outer surface of the particle, the mass passed outside the particle for any fission product is:

$$r = \int \int -D \nabla C \cdot n \, \mathrm{d}t \, \mathrm{d}A \tag{9}$$

where D is the Arrhenius diffusion coefficient for the given fission product (see Section 2.1.2), C represents the concentration of the fission product, n is the vector normal to the exterior surface, and A is the outer surface of the particle.

The total fission product production is:

$$p = \int \int \Gamma \dot{F} \, \mathrm{d}t \, \mathrm{d}V \tag{10}$$

where Γ is the fission yield (atom/fission), $\dot{F}$ is the fission rate (fission/m^3-s), and V represents the volume of the fuel kernel.

The release fraction is defined as

$$f = \frac{r}{p}. \tag{11}$$

3. Verification

Verification is the software development process for assuring that the code contains no programming errors and that it computes correct solutions for carefully designed problems. This section discusses code verification, a mathematically rigorous approach that includes a demonstration of computing the correct solution to a prescribed problem using a series of more refined an meshes.

3.1. Code verification

A formal proof that an analysis ran correctly is generally impossible because the expected code output cannot be precisely determined [11]. This is due to the fact that code results are dependent upon many factors (e.g., the selected numerical algorithm, temporal/spatial discretization, iterative tolerances, machine precision, etc.). In the absence of a formal proof of correctness, code verification can instill confidence in the correctness of a scientific code. This is achieved through a quantified demonstration that the code results converge to a reference solution at the theoretical rate as the computational mesh and time discretization are refined.

Selection of a reference solution is the first task in the verification procedure. Here, we employ two methods for code verification:

1. The *method of exact solutions (MES)* [12], in which a known solution to the intended mathematical model is found as some nonlinear system operator ($\mathcal{L}$) (Eq. (12)):

$$\mathcal{L}[f(\vec{x}, t)] = 0 \tag{12}$$

   where the solution, $f(\vec{x}, t)$, is a function of space ($\vec{x}$) and time (t).
   Finding a non-trivial analytic solution to a complex nonlinear differential equation is difficult. The solution to such equations often requires significant simplifying assumptions. For example, many analytic solutions require that one or more terms in the partial differential equation (PDE) be trivial and thus eliminated from the solution. This process becomes even more difficult when a system of nonlinear equations is considered.
2. The *method of manufactured solutions (MMS)* [11–14], in which we manufacture a particular form of the solution $M(\vec{x}, t)$ and then seek the necessary source term, $Q(\vec{x}, t)$, that would result in the manufactured solution:

$$\mathcal{L}[M(\vec{x}, t)] = Q(\vec{x}, t). \tag{13}$$

   The source term, $Q(\vec{x}, t)$, is implemented in the simulation tool, and then the verification process is performed. This methodology requires that the manufactured solution is formulated using continuous, smooth functions sufficiently complex to reveal nonlinearity in the governing equations. The chosen manufactured solution can be physically unrealistic, as it is intended only to test the underlying numerical algorithms.

Any necessary boundary conditions or initial conditions can be derived directly from the manufactured solution $M(\vec{x}, t)$. Any equations of state, varying properties, or nonlinear sources can be incorporated into the method of manufactured solutions (MMS) process by implementing them in the nonlinear operator $\mathcal{L}$. This allows all relevant code options to be tested in different combinations. In addition, MMS does not require the complex analytic solutions formed for method of exact solutions (MES), greatly reducing the labor required for the verification process.

The theoretical rate of convergence (or the formal order of accuracy) can be determined through an analysis of the linear truncation error (LTE). After we select the method to obtain solutions, the theoretical convergence rate of the numerical algorithm is established. Then, a numerical representation of the mathematical model is formulated and solved on at least three consecutive meshes. Global errors between the numerical solutions and the reference solution are calculated using error norms. For example, the L_2 norm (or Euclidean norm) of the error over the solution domain Ω is defined as:

$$||q|| = \left[\int_\Omega (q - \tilde{q})^2 \mathrm{d}\Omega\right]^{1/2} \tag{14}$$

where the reference solution is represented by the primary variable q (e.g., temperature for heat conduction, displacement for mechanics, etc.) and the numerical approximation is $\tilde{q}$. All of the above arguments can also be applied to the flux, ∇q, with the norm becoming the H_1 norm. Since the flux involves the first derivative of q, its convergence rate is one order lower than that of the function.

The local LTE converges at some rate; therefore, the global error will converge at the same rate if the mesh size is (1) small enough to eliminate higher-order LTE terms and (2) large enough that numerical error is not dominant. To relate the error to the characteristic element size h, we use the following:

$$||q|| = Ch^{\hat{p}} \tag{15}$$

where C is a problem-dependent constant and $||\cdot||$ indicates a norm. $\hat{p}$ is the observed order of accuracy. Using the L_2 norm, the expected order is $\hat{p} = p + 1$, and using the H_1 norm, the expected order is $\hat{p} = p$ where p is 1 for the first-order or linear an and 2 for the second-order or quadratic an. Eq. (15) is in a power law form; therefore, the slope of the error on a log-log plot is

$$\hat{p} = \frac{\log\left(||q||_{rh}/||q||_h\right)}{\log(r)} = \log_r\left(\frac{||q||_{rh}}{||q||_h}\right) \tag{16}$$

where $||q||_h$ is the norm of q at some mesh size (h) and r is the mesh refinement factor ($r \geq 2$). More details on the formal order of accuracy of the finite element method can be found in [15,16].

The code verification exercise is successful if the observed order of accuracy matches the formal order of accuracy. This provides confidence in the implemented numerical algorithm. Then, the problem is used as supporting evidence that the particular combination of physics, discretization, geometry, boundary conditions, and initial conditions is free of coding mistakes.

3.2. Demonstration

In this work, we demonstrate each method via a single problem: Problem 3.1 for the MES and Problem 3.2 for the MMS.

Problem 3.1. A solid sphere has spatially dependent internal heating:

$$q''' = q'''_o\left(1 - \beta\frac{r^2}{r_o^2}\right) \tag{17}$$

where the radius of the sphere is r_o ($0 \leq r \leq r_o$) and k is the constant thermal conductivity. It has a constant temperature imposed on its boundary: $T(r = r_o) = T_o$. The sphere reaches thermal equilibrium, and the analytic solution for the temperature distribution is [17,18]:

$$T(r) = T_o + \frac{q'''_o r_o^2}{6k}\left[\left(1 - \frac{r^2}{r_o^2}\right) - \frac{3\beta}{10}\left(1 - \frac{r^4}{r_o^4}\right)\right]. \tag{18}$$

This problem is obtained from [15] and solved in BISON on the domain $\vec{X} \in [0, 1]$. The center of the sphere uses a Neumann boundary condition (finiteness requirement), and the surface has a Dirichlet condition: $(dT/dr)_{r=0} = 0$ and $T(1) = T_R = 300K$. Steady-state heat conduction is considered in the sphere with constant thermal conductivity $k = 1W/m/K$. The analytical solution is shown in Fig. 4a.

Problem 3.2. Fick's second law of diffusion follows the same mathematical model as the heat equation. A PDE with constant material properties can be written as:

$$\frac{\partial u}{\partial t} = \kappa\nabla^2 u + Q \tag{19}$$

where u is temperature and κ is thermal diffusivity for the heat conduction equation and where u is concentration and κ is the diffusion coefficient for the diffusion equation. Q is the source term.

Here, we analyze a steady-state one-dimensional heat conduction (or diffusion) equation in spherical coordinates using the manufactured solution:

$$u(r) = \sin(a\pi r). \tag{20}$$

This simple function is suitable for use in an MMS problem because it is continuous and infinitely differentiable. To find the source term, Q, that produces the solution, u, the steady-state heat conduction operator $\mathcal{L} = -\nabla\cdot\nabla$ is applied to u. With $\kappa = 1$, this results in the following source term:

$$Q = \mathcal{L}(u) = -\frac{2a\pi}{r}\cos(a\pi r) + a^2\pi^2\sin(a\pi r). \tag{21}$$

The problem is solved with BISON over the domain $\vec{X} \in [0, 1]$. The manufactured solution is shown in Fig. 5a using $a = 2$, which is the value used in the BISON implementation. Steady-state heat conduction is considered through a homogeneous solid using the external source in Eq. (21). Dirichlet boundary conditions are derived from the manufactured solution using $a = 2$.

Results & Discussion The exact and computed solutions in Fig. 4a for Problem 3.1 and Fig. 5a for Problem 3.2 are shown for three different meshes and two an types (first order, or linear, with two nodes per element; second order, or quadratic, with three nodes per element). A convergence study is conducted with a refinement factor of two ($r_r = 2$). The computed norms for each an type are plotted in Fig. 4b for Problem 3.1 and Fig. 5b for Problem 3.2. Note that the L_2 norm quantifies the convergence of the temperature distribution (*solid lines*) and the H_1 norm quantifies the convergence of the heat flux (*dashed lines*). Slopes of first-, second-, and third-order convergence are indicated. The formal order of accuracy is two for linear ans and three for quadratic ans for the temperature solution and one less in each case for the heat flux solution. In the asymptotic region for both cases, the linear and quadratic an solutions converge to the exact solution with the correct order of accuracy. Note that for Problem 3.1 with quadratic elements, numerical error begins to pollute the solution when the mesh is refined greatly. This is a common occurrence with very fine meshes.

These results show that the implementation of the heat equation (and the diffusion equation) with one-dimensional finite elements is correct in BISON. For BISON results for similar verification problems, see [15,16].

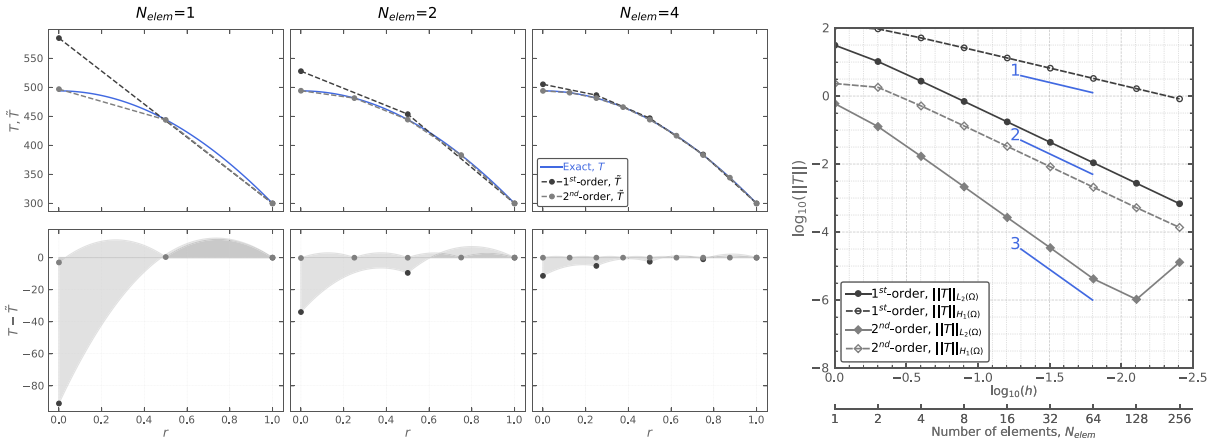

(a) Temperature distributions (*first row*) and residual (*second row*) for different meshes and finite elements.

(b) Convergence plot (r_r = 2).

Fig. 4. BISON results for Problem 3.1 using one-dimensional finite elements.

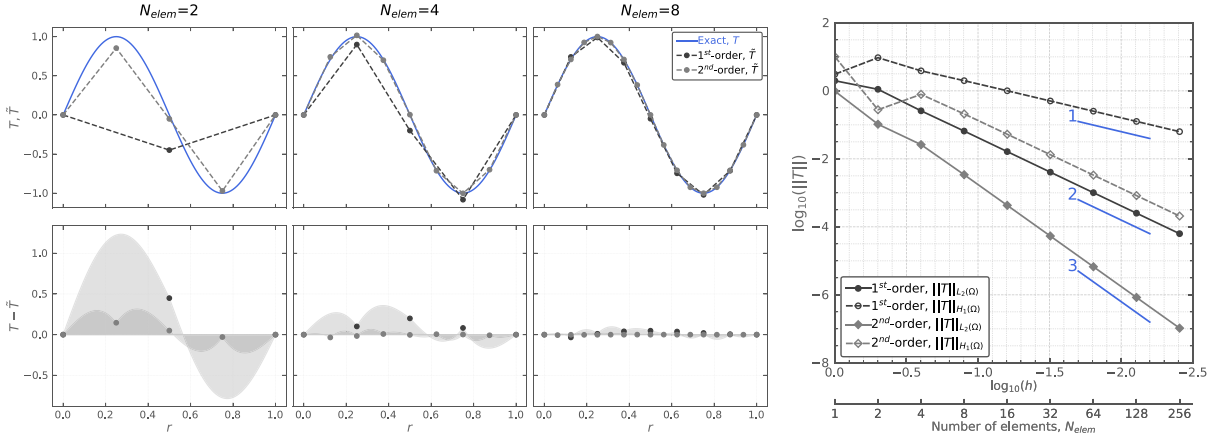

(a) Temperature distributions (*first row*) and residual (*second row*) for different meshes and finite elements.

(b) Convergence plot (r_r = 2).

Fig. 5. BISON results for the Problem 3.2 using one-dimensional finite elements.

4. Benchmarking: CRP-6

The IAEA-sponsored CRP-6 explored the modeling of TRISO fuel as part of a larger effort to promote "the exchange of technical information...in the field of gas cooled reactors." In particular, CRP-6 organized "two specific benchmark exercises with the application of HTGR fuel performance and fission product release codes which helped compare the quality and validity of the computer models against experimental data and also against each other" [2]. These benchmark calculations were completed just as BISON was begun and have served as very valuable references for the calculation of both fuel performance and fission product diffusion in TRISO fuel.

This section compares BISON results to results from the CRP-6 exercises. We begin by revisiting cases that were previously run with BISON and then discuss the remaining cases.

4.1. Previously run fuel performance cases: 1–8, 10, 11

Regarding the fuel performance benchmark cases, three of these were simple enough to have analytical solutions using elastic material models. The others were more complex, using nonlinear material models and increasingly realistic boundary conditions. Several of these cases were originally run with BISON as part of [1]. Here, we present those results, along with results using the current version of BISON. Small differences are seen in the results between the original BISON calculations and the current calculations due to minor changes in modeling practices. All current results reported here use one-dimensional ans with spherical symmetry. Details on all the cases are available in [1,2].

Table 2
Comparison of analytical solution values for maximum tangential stress (MPa) to original ([1]) and current BISON results for Cases 1–3.

Case	Layer	Analytical	Original	Error (%)	This study	Error (%)
1	SiC	125.190	125.230	0.032	125.130	0.048
2	IPyC	50.200	50.287	0.173	50.176	0.048
3	IPyC	8.800	8.700	1.140	8.700	1.140
	SiC	104.400	104.500	0.100	104.500	0.100

The first three cases, as mentioned, have simple elastic material models. Case 1 has a single SiC layer, Case 2 has a single PyC layer, and Case 3 has an inner PyC layer and a SiC layer. Results are shown in Table 2. The results match the analytical values very well.

Cases 4a, 4b, 4c, 4d, 5, 6, and 7 involve inner pyrolytic carbon (PyC) (IPyC) and SiC layers. Results are in Table 3. In every case, the results are within the ranges of values reported by the CRP-6

Table 3
Comparison of the range of values reported by CRP-6 participants to original ([1], blue marker) and current BISON (red marker) results for Cases 4a–7.

Case	Layer	CRP-6 codes	BISON predictions	
4a	IPyC	[925, 970]	Original	928.0
			This study	925.0
	SiC	[-850, -775]	Original	-819.0
			This study	-816.0
4b	IPyC	[-25, -25]	Original	-25.0
			This study	-25.0
	SiC	[138, 142]	Original	139.0
			This study	139.0
4c	IPyC	[25, 27]	Original	26.0
			This study	25.8
	SiC	[83, 92]	Original	89.4
			This study	89.2
4d	IPyC	[25, 35]	Original	27.8
			This study	30.3
	SiC	[71, 88]	Original	87.0
			This study	84.5
5	IPyC	[40, 58]	Original	41.9
			This study	44.2
	SiC	[-56, -28]	Original	-32.2
			This study	-32.1
6	IPyC	[27, 38]	Original	29.2
			This study	31.4
	SiC	[28, 48]	Original	44.9
			This study	41.9
7	IPyC	[37, 50]	Original	38.0
			This study	42.5
	SiC	[10, 25]	Original	24.6
			This study	21.7

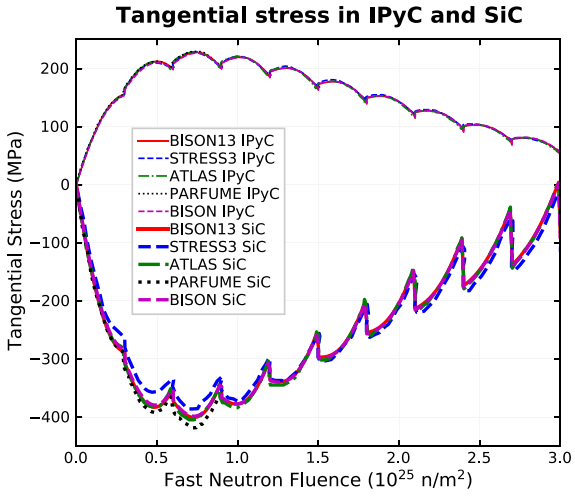

Fig. 6. Comparison of code results for inner-wall tangential stress in IPyC and SiC for Case 8. Both the original (BISON13 [1]) and current BISON results match those of other codes very well.

participants. As noted in [1], values in the ranges were extracted from plots in [2].

For Case 8, the particle temperature was ramped between 873 and 1273 K, a total of ten times. Results from this analysis are in Fig. 6. The BISON results match those of other codes extremely well.

The final two cases in the CRP-6 set originally run with BISON are Cases 10 and 11. These cases are quite different from the cases already discussed. For Cases 10 and 11, the particle's internal pressure was set by the fission gas release (FGR) and carbon monoxide (CO) production models in the individual codes. Since different codes used different models for FGR and CO production, the codes produced fairly different results. Results for gas pressure and tangential stress in the silicon carbide (SiC) layer are in Fig. 7. The BISON results compare well to the range of results from other codes.

Table 4
Comparison of the range of values reported by CRP-6 participants to BISON (red marker) results for Case 1, fractional release of cesium from a bare kernel.

Case	CRP-6 codes	BISON predictions	
1a	[0.453, 0.498]	This study	0.466
1b	[0.970, 1.000]	This study	1.000

4.2. New fuel performance cases: 9, 12, 13

The remaining fuel performance cases of CRP-6–Cases 9, 12, and 13–are similar to Cases 10 and 11. For these three cases, the mean particle geometry, burnup level, and fluence level are prescribed, along with material properties. FGR and CO production are left to the analysis teams. Given the differences in those models, differences in gas pressure and tangential stress in the SiC layer are expected.

Case 9 has a fuel radius of 272 μm, with 89 days of irradiation to reach 4.79% fissions per initial metal atom (FIMA) and a fluence of 2.1×10^{25} n/m^2. Results are shown in Fig. 8. The BISON results are comparable to those of other codes.

Case 12 is somewhat unique among the CRP-6 benchmark cases in that (1) its fuel is uranium oxicarbide (UCO) rather than UO_2 and (2) the fuel is highly enriched. The fuel radius is 100 μm and reaches 79% FIMA and a fluence of 3.8×10^{25} n/m^2 in 170 days of irradiation. Results are shown in Fig. 9. The BISON results are comparable to those of other codes.

Case 13 has a fuel radius of 251 μm and reaches 20% FIMA and a fluence of 5.4×10^{25} n/m^2 in 600 days of irradiation. Results are shown in Fig. 10. The BISON results are comparable to those of other codes.

4.3. Diffusion cases

CRP-6 also includes a set of cases intended to exercise diffusion capabilities. These cases included a set based on assumed model parameters (Cases 1–5), along with a set based on heating tests (Cases 6–11). In all the cases, the diffusion of one or more fission products is measured via the fractional release (ratio of a given fission product released from the particle to the amount produced, Eq. (11)).

Diffusivities for these cases follow the German models given in [10]. Table 1 is based on these models. The German model for the diffusivity of cesium in SiC is a function of fast neutron fluence. Fig. 11 shows diffusivities of cesium, strontium, and silver for kernel, buffer, pyrolitic carbon and silicon carbide materials.

Cases 1a and 1b are for the diffusion of preexisting cesium in a bare kernel. Case 1a has a temperature of 1200 °C, and Case 1b has a temperature of 1600 °C. The simulation time is 200 h for both cases. Results are shown in Table 4.

Cases 2a and 2b are similar to 1a and 1b except that the particle includes the kernel, buffer, and inner PyC. Results are in Table 5.

Similar to Cases 1 and 2, Case 3 evaluates the diffusion of preexisting fission products. Case 3, however, involves a complete TRISO particle. In Case 3a, the temperature is 1600 °C held for 200 h. In Case 3b, the temperature is 1800 °C for 200 h. In Case 3c, the temperature is 1600 °C for 200 h, followed by a temperature of 1800 °C for 200 h.

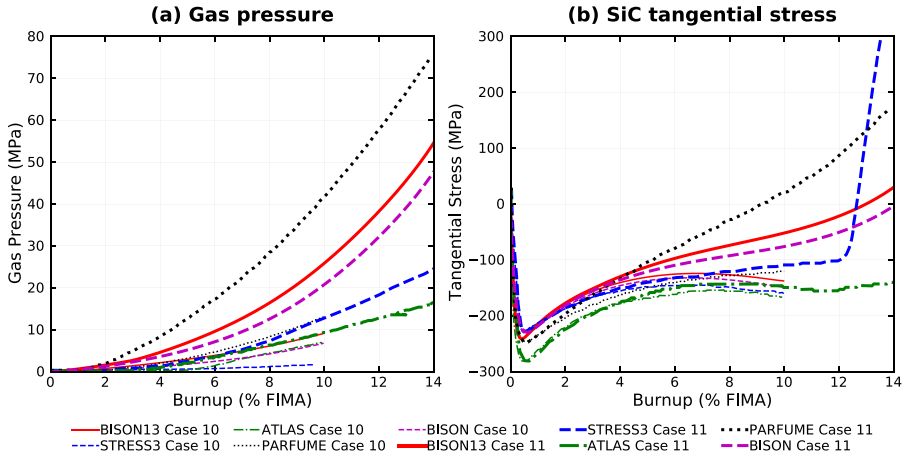

Fig. 7. Results for Cases 10 and 11. Both the original (BISON13 [1]) and current BISON results are within the range of results from other codes.

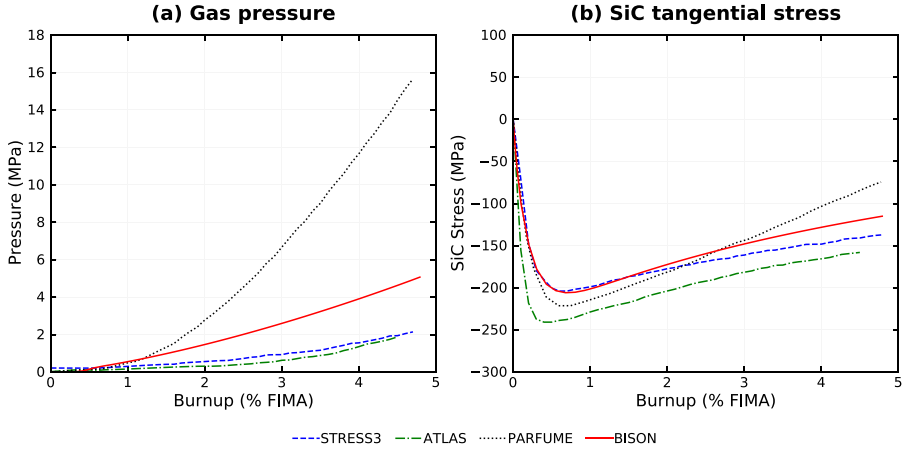

Fig. 8. Results for Case 9. Results from other codes extracted from [2].

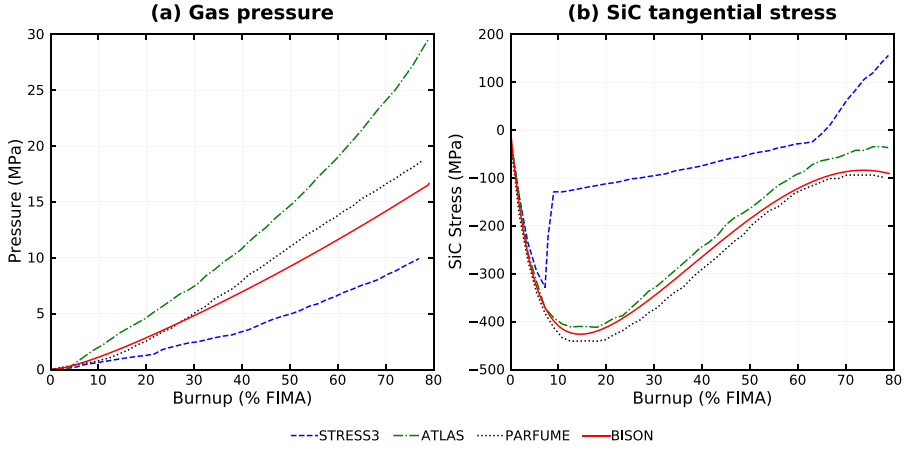

Fig. 9. Results for Case 12. Results from other codes extracted from [2].

Cases 3d and 3e have the same temperature conditions as Case 3c. In Case 3d, the SiC layer cracks at 1800 °C. In Case 3e, the SiC layer cracks at 1600 °C, and the inner and outer PyC layers crack at 1800 °C. Cracked layers have their diffusivities set to 1×10^{-6} m^2/s.

Results for Case 3 are in Table 6.

Case 4 does not involve a preexisting inventory of fission products. Instead, fission products are built up over 500 days of irradiation at 1000 °C, reaching a burnup of 10% FIMA and a fast neutron fluence of 2×10^{25} n/m^2. Case 4a ends with 200 h at 1600 °C, and Case 4b ends with 200 h at 1800 °C. Case 4c has 200 h at 1600 °C, followed by 200 h at 1800 °C. Case 4d is much like Case 4c, but

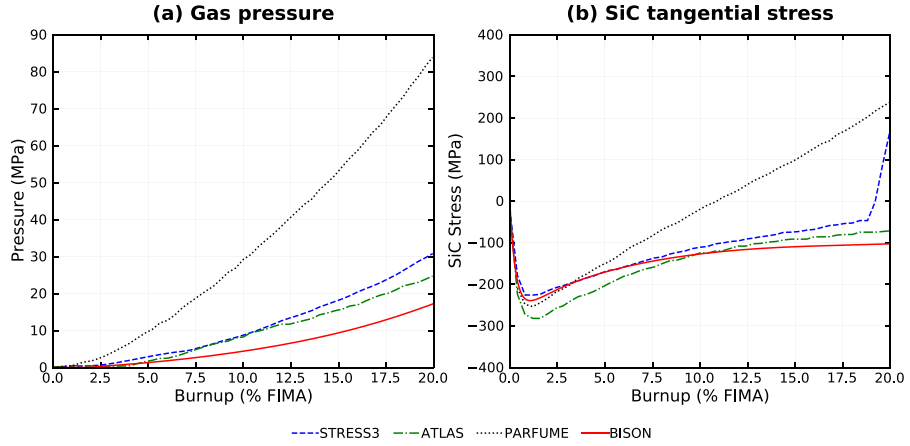

Fig. 10. Results for Case 13. Results from other codes extracted from [2].

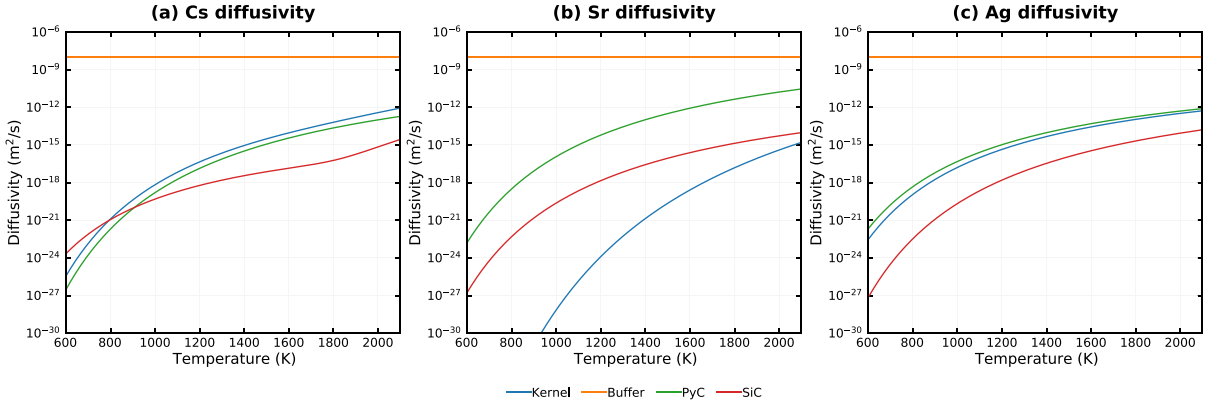

Fig. 11. Diffusivities of cesium, strontium, and silver in kernel, buffer, pyrolytic carbon, and silicon carbide (fast neutron fluence is $5.5 \times 10^{25} n/m^2$) [10].

Table 5
Comparison of the range of values reported by CRP-6 participants to BISON (red marker) results for Case 2, fractional release of cesium from the kernel, buffer, and inner PyC.

Case	CRP-6 codes	BISON predictions		
2a	[0.006, 0.030]	This study	0.027	[I]
2b	[0.968, 0.996]	This study	0.995	[I]

Table 6
Comparison of the range of values reported by CRP-6 participants to BISON (red marker) results for Case 3, fractional release of cesium from the TRISO particle.

Case	CRP-6 codes	BISON predictions		
3a	$[6.59 \times 10^{-5}, 1.13 \times 10^{-3}]$	This study	1.33×10^{-4}	[I]
3b	[0.203, 0.218]	This study	0.210	[I]
3c	[0.220, 0.239]	This study	0.225	[I]
3d	[0.999, 1.000]	This study	1.000	[I]
3e (Cs)	[0.970, 1.000]	This study	1.000	[I]
3e (gases)	[0.980, 1.000]	This study	1.000	[I]

the SiC layer cracks at 1600 °C, and the inner and outer PyC layers crack at 1800 °C. Cracked layers have their diffusivities set to 1×10^{-6} m^2/s.

Results for Case 4 are in Table 7.

Table 7
Comparison of the range of values reported by CRP-6 participants to BISON (red marker) results for Case 4, fractional release of cesium and silver from the TRISO particle with 500 days of irradiation.

Case		CRP-6 codes	BISON predictions		
Cs	4a	$[1.64 \times 10^{-4}, 1.47 \times 10^{-3}]$	This study	2.44×10^{-4}	[I]
	4b	[0.20, 0.23]	This study	0.20	[I]
	4c	[0.21, 0.24]	This study	0.22	[I]
	4d	[1.00, 1.00]	This study	1.00	I
Ag	4a	[0.27, 0.55]	This study	0.38	[I]
	4b	[0.58, 0.95]	This study	0.78	[I]
	4c	[0.92, 0.98]	This study	0.90	I [ ]
	4d	[0.98, 1.00]	This study	1.00	[I]

Like Case 4, Case 5 builds up fission products over a period of irradiation. In Case 5, the irradiation period is 1,000 days. That time is divided into 10 cycles, during which the temperature ramps up from 600 to 1000 °C for each cycle. The final burnup is 10% FIMA, and the final fast neutron fluence is 2×10^{25} n/m^2. Case 5a considers cesium and silver diffusion after 1,000 days, while Case 5b adds 200 h at 1600 °C.

Results are in Table 8.

The results from Cases 1 through 5 demonstrate that BISON's predictions of fission product diffusion in TRISO fuel particles compare very well to those of other codes, providing evidence that BISON's diffusion calculations meet expectations.

Table 8
Comparison of the range of values reported by CRP-6 participants to BISON (red marker) results for Case 5, fractional release of cesium and silver from TRISO particle with 10 cycles of irradiation.

Case		CRP-6 codes	BISON predictions		
Cs	5a	$[2.19 \times 10^{-19}, 1.92 \times 10^{-11}]$	This study	2.45×10^{-18}	[ ]
	5b	$[3.07 \times 10^{-4}, 1.22 \times 10^{-3}]$	This study	1.49×10^{-4}	[ ]
Ag	5a	$[5.55 \times 10^{-6}, 5.06 \times 10^{-5}]$	This study	6.51×10^{-6}	[ ]
	5b	[0.14, 0.54]	This study	0.40	[ ]

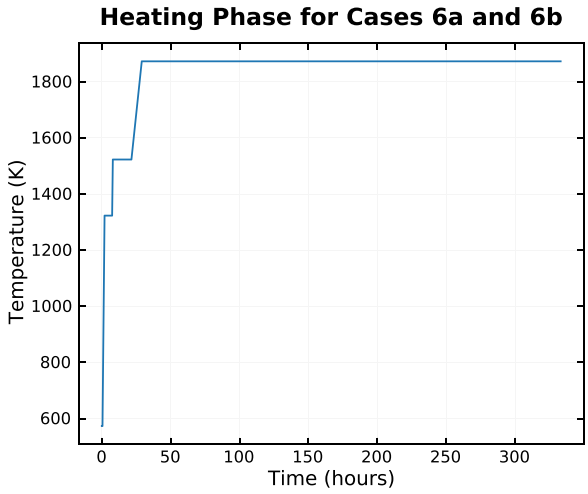

Fig. 12. Temperature during heating phase for Cases 6a and 6b.

The next set of diffusion cases, Cases 6–11, is based on heating tests. After a period or irradiation, furnace heating is simulated via a prescribed, elevated temperature boundary condition. [2] describes Cases 6 through 9 as "postcalculation" studies, since they are based on experiments conducted previously. Cases 10 and 11 are considered "prediction" cases, since those cases are based on experiments that were planned but not complete.

In the plots below, experimental data and results from other codes were digitized based on plots in [2].

Case 6a was irradiated for 351 effective full-power days (EFPD) at 940 °C. This was followed by a heating period of 333 h containing three ramps reaching a final temperature of 1600 °C. Fig. 12 shows the prescribed temperature during the heating phase. (Subsequent cases have similar heating phases; see [2] for details.) Plots of cesium, silver, and strontium fractional release are in Fig. 13.

For each case, the report [2] lists ranges of dimensions for the kernel diameter and buffer, IPyC, SiC, and OPyC thicknesses. A statistical study of Case 6a was run using a Latin hypercube approach to generate 1,000 realizations of the particle. From those 1,000 realizations, the mean and standard deviation values of fractional release were computed. Results are shown in Fig. 14. From these plots, it is clear that the fractional release computed using the mean geometrical values is nearly identical to the fractional release computed as the mean of a large sample of realizations spanning the variations in geometry, as anticipated. This shows that for the purposes of large population diffusion, the layer thickness variation has only a small effect, at least for the parameters in [2]. Thus, for the remaining CRP-6 diffusion cases, only calculations using the mean geometrical values were performed.

Again using Case 6a, the sensitivities of fractional release were computed based on a statistical sampling of the dimensions of the kernel, buffer, IPyC, SiC, and OPyC layers over the ranges listed in [2]. The sensitivities are given in Fig. 15. The negative values in the figure show that, for all species, increasing the thickness of a given layer decreases fractional release. For cesium, the SiC layer is clearly the most significant layer. Silicon carbide is the most important layer for strontium and silver as well, though the thickness of other materials is also important. Diffusivity in the buffer layer is orders of magnitude higher than in other layers. However, increasing the buffer layer thickness increases the volume of the pyrolytic carbon and SiC layers, resulting in lower release. The effectiveness of the OPyC layer in controlling release is very small. Fission products that have diffused through the SiC layer will diffuse through the OPyC layer quickly.

Case 6b is similar to Case 6a, except that the irradiation temperature, final burnup, and final fast neutron fluence are higher. Case 6b also includes three failed particles, each assumed to have failed at a different time during the highest temperature portion of the heating phase. To compute the net fractional release, a weighted average was used:

$$x = \frac{1}{n}\left((n - n_f)x_0 + \sum_{i=1}^{n_f} x_i\right) \tag{22}$$

where x is the net fractional release, n is the total number of particles, n_f is the number of failed particles, x_0 is the fractional release for an intact particle, and x_i for $i = 1..n_f$ is the fractional release of the ith failed particle. For this test, $n = 1631$.

Plots of cesium, strontium, and silver fractional release for Case 6b are in Fig. 16.

Case 7a was irradiated for 88.9 EFPD at an average temperature of 1031 °C. A total heating period of 277 h followed, with a maximum temperature of 1700 °C. Plots of cesium and silver fractional release are in Fig. 17.

Case 7b is different from Case 7a in that the heating phase is a total of 222 h with a maximum temperature of 1800 °C. Plots of cesium and silver fractional release for Case 7b are in Fig. 18.

Case 8a involves an irradiation period of 359 EFPD. In contrast to other cases, both a surface and a center temperature were given for this case. In our analysis, we use the surface temperature throughout the particle. This case includes a 500-hour heating phase with a peak temperature of 1600 °C. Plots of cesium, silver, and strontium fractional release are in Fig. 19.

Case 8b was irradiated at a lower temperature but to a higher burnup and fast neutron fluence than Case 8a. The heating phase lasted 187 h and contained two periods at 1800 °C. Ten particles were assumed to have failed during the 1800 °C phase (out of 16,350 total). Eq. (22) was used to compute the net fractional release for cesium, strontium, and silver. Results are in Fig. 20.

The particle in Case 9 was irradiated for 634 EFPD. The heating phase included two peaks at 1800 °C. Five particles were assumed to have failed out of 14,580 particles total. Eq. (22) was used to compute the net fractional release. Results for cesium and silver are in Fig. 21.

Case 10 was developed as its corresponding experiment was in planning. Since that time, experimental data has become available [2]. The particle was irradiated for 249 EFPD, with a total heating time of 836 h, with 200 h at 1800 °C. It was assumed that no particles failed. Results for Case 10 are in Fig. 22.

Case 11 was developed entirely as a code benchmarking exercise. It involves hours at 1800 °C was chosen to conclude the heating phase. Only results irradiation for 1,000 EFPD and 824 h of heating phase. Again, 200 for cesium are available, which are plotted in Fig. 23.

Based on the results from Cases 6–11, the following general observations are made:

- Results from participants show considerable scatter.
- Results from participants show greater agreement toward the end of the heating phases.

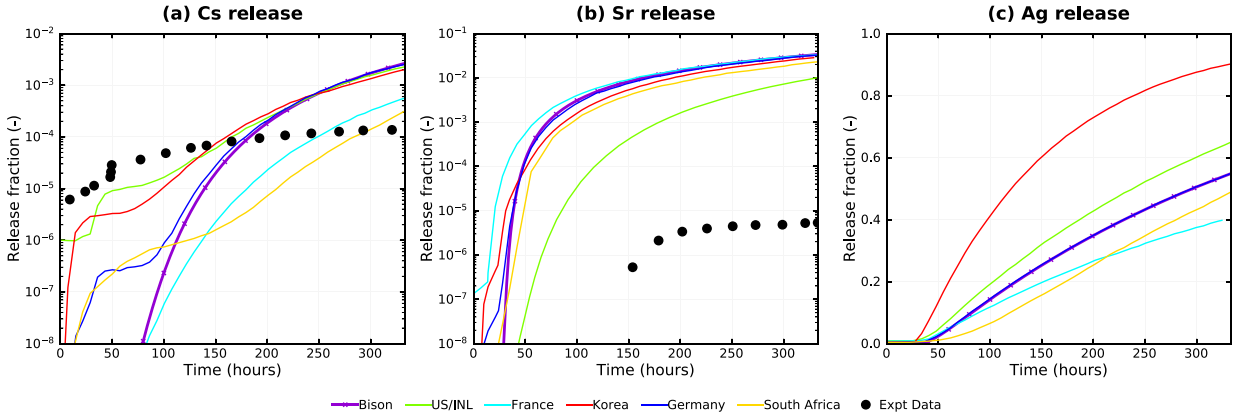

Fig. 13. Release fractions for Case 6a.

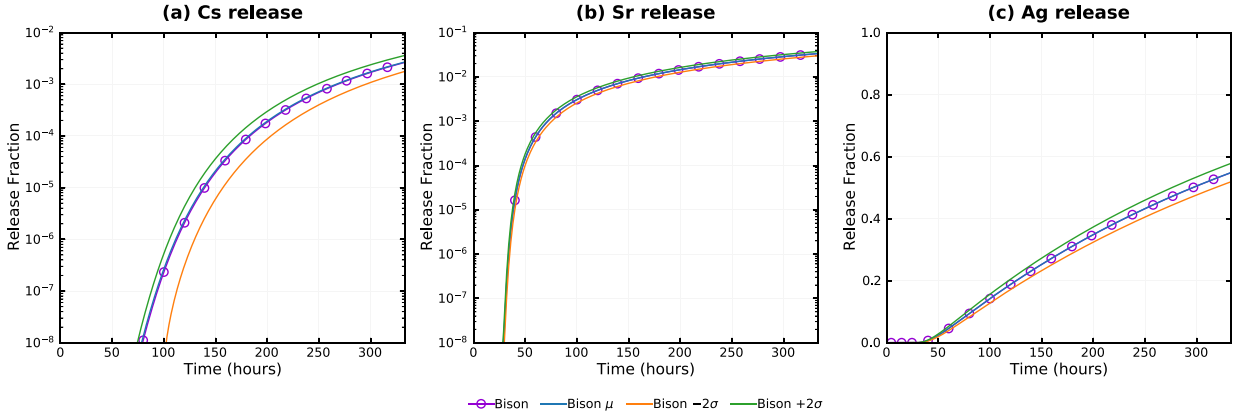

Fig. 14. Release fractions for Case 6a using values from 1,000 samples.

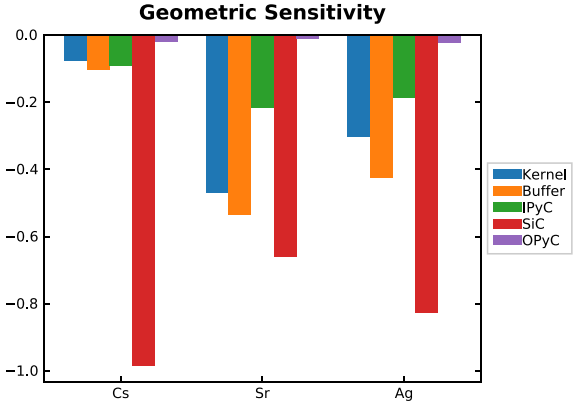

Fig. 15. Sensitivity of fractional release to size of each layer in Case 6a. Negative values indicate that greater thickness decreases fractional release. The most dominant layers are indicated by the longest bars.

- BISON results are comparable to results from other participants.
- With a few exceptions, predicted fractional release is considerably higher than observed fractional release.
- BISON results most closely match those from Germany, particularly for silver.

The CRP-6 benchmark cases have been extremely valuable as a means of exercising BISON's TRISO capabilities and determining best practices for particle analysis. That BISON's results match published results so well, for both stress and diffusion, is evidence that the relevant equations were coded correctly and that adequate meshes and numerical techniques were used.

5. Validation

Validation is the software development process for determining whether computed values match real-world conditions. It is the process of comparing code results to experimental data and is an essential part of determining whether a code is suitable for use as a design tool. This section discusses fission product diffusion validation based on AGR-1 data.

DOE's Advanced Gas Reactor program sponsored a series of irradiation tests on TRISO particle fuel. The first of these, AGR-1, included PIE of the release of silver, cesium, and strontium. The details of AGR-1 are documented elsewhere (see [3] and the references therein), so only a brief orientation is given here.

The AGR-1 experiment was configured in capsules. Each capsule housed 12 fueled compacts as three stacks of four vertically aligned compacts. At six capsules, the experiment included a total of 72 compacts, each identified by a capsule number, vertical level within the capsule, and stack number. Irradiation conditions, including power level and compact-average temperature, are available for each day of irradiation.

The analysis procedure is as follows. Given that power and temperature are known only as average values at the compact level, a single particle is analyzed for each compact. The internal temperature of the particle depends on the power level, which provides an energy input due to fission in the fuel kernel, and the temperature

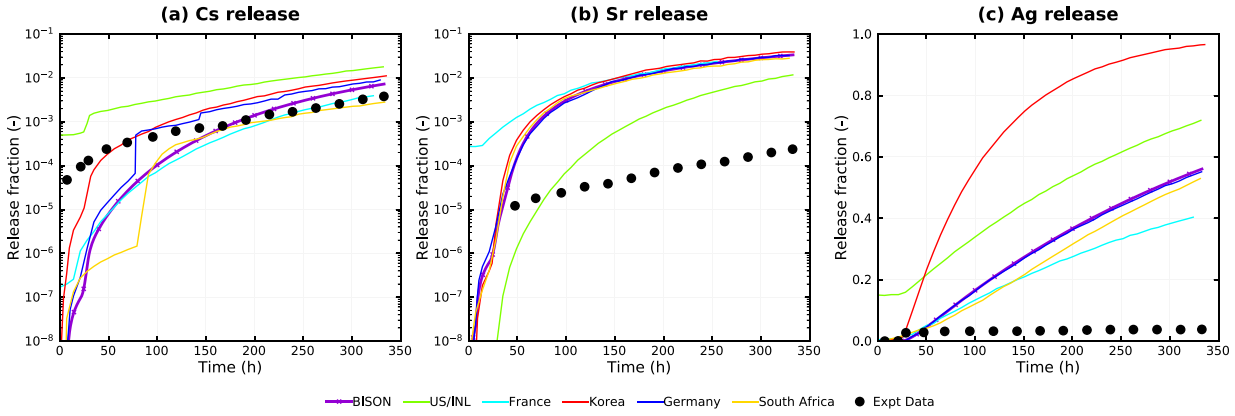

Fig. 16. Release fractions for Case 6b.

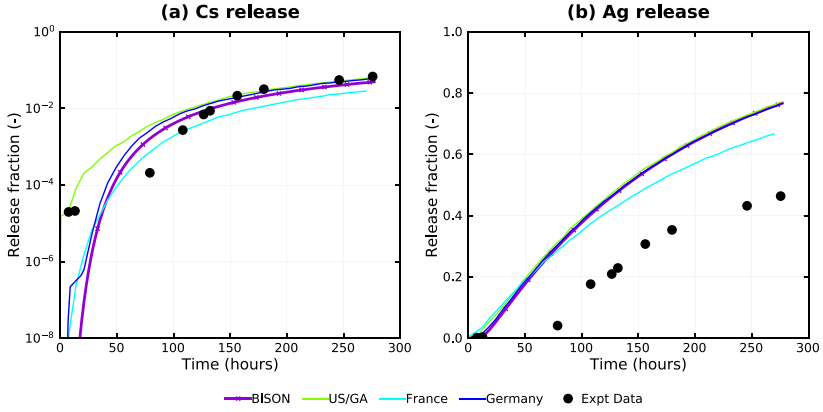

Fig. 17. Release fractions for Case 7a.

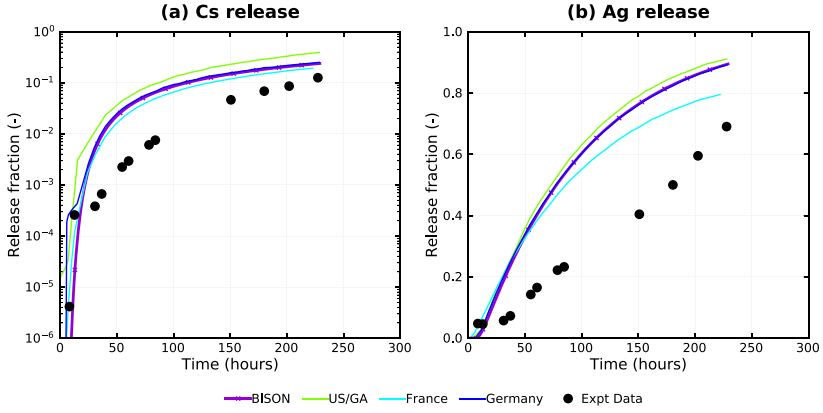

Fig. 18. Release fractions for Case 7b.

at the outer surface of the particle, which is set to the compact average temperature. Fission product transport depends on diffusion coefficients (see Section 2.1.2), fission yields (see Section 2.1.3), and the computed temperature. The diffusion coefficient in the compact outside the particles is high enough to justify the assumption that all fission products that left the particles will have left the compacts also.

The comparisons that follow for silver, cesium, and strontium are among the first fission product diffusion validation results using BISON for TRISO analysis. Other researchers have done similar work [19], but those results have not been independently checked and added to the BISON code repository.

5.1. Silver release

To compare experimentally measured release fractions of silver, we follow the approach in [3]. In particular, we analyzed the 17 compacts listed in Table 3 of that work and plotted the results in a manner similar to its Fig. 5. Our results, shown in Fig. 24, include values from PIE, PARFUME, and BISON. As seen from the figure, the BISON results compare very favorably with the PARFUME results.

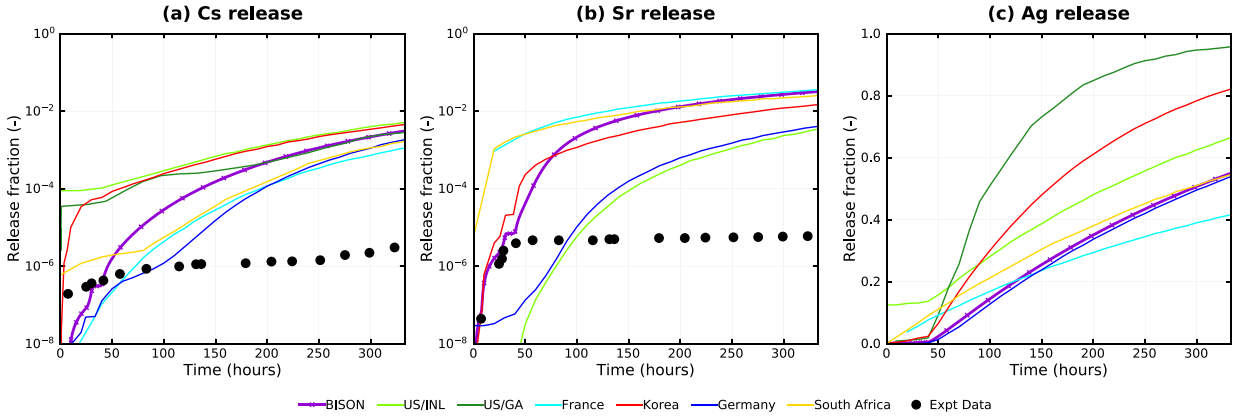

Fig. 19. Release fractions for Case 8a.

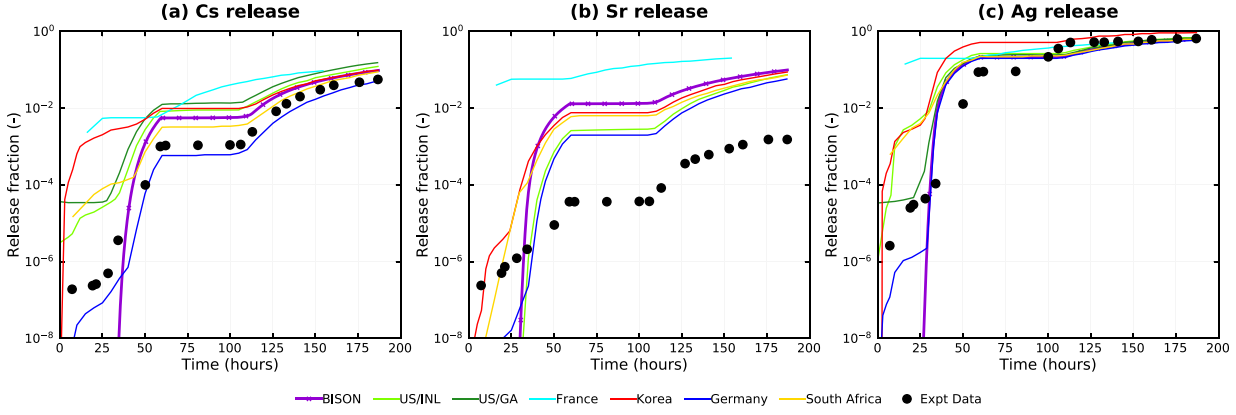

Fig. 20. Release fractions for Case 8b.

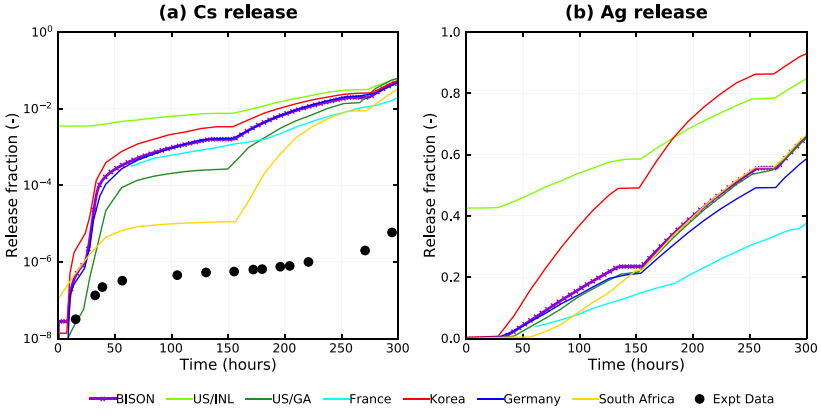

Fig. 21. Release fractions for Case 9.

Fig. 25 shows the concentration of silver in Compact 6-1-1 growing significantly over time. The sharp drop in concentration at about 0.8 r/r_0 is due to the low diffusivity of silver in SiC.

Note that the calculation of silver release in this section (and of cesium and strontium) relies on effective fission yields and does not consider decay. This is done to follow the approach in [3] and allows valid comparisons to PARFUME data.

5.2. Cesium and strontium release

The evaluation of cesium and strontium release mostly follows the same approach as for silver release. However, the comparisons for each fission product are made in two parts. In one set of comparisons, only compacts with no known particle failures are included. In the other set, compacts with either one or two failed particles are included.

The analysis procedure for compacts with no known particle failures is exactly the same as that described for silver.

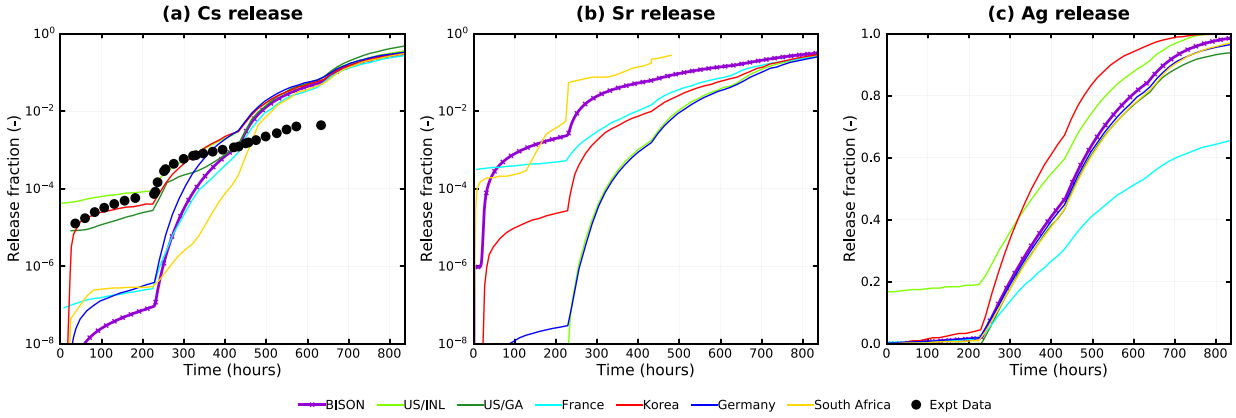

Fig. 22. Release fractions for Case 10.

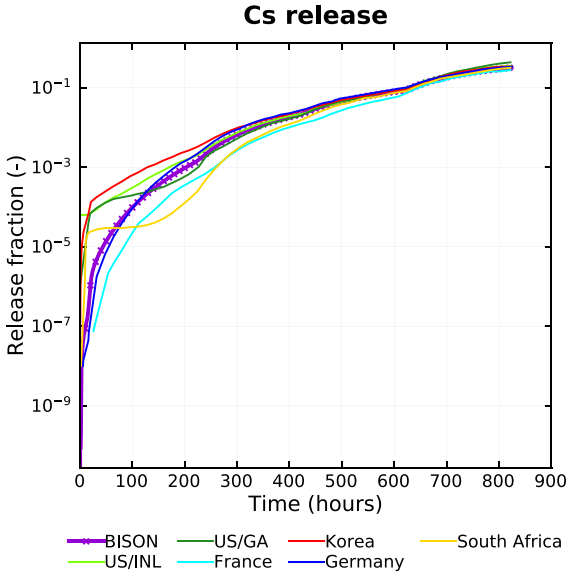

Fig. 23. Release fractions for Case 11.

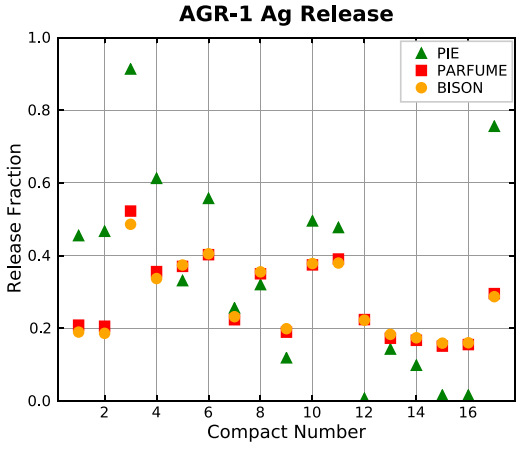

Fig. 24. Comparison of measured and computed silver release fractions for seventeen compacts (6-4-3, 6-4-1, 6-2-1, 6-1-1, 5-3-3, 5-2-3, 5-1-3, 5-3-1, 4-4-3, 4-3-3, 4-3-2, 4-1-2, 4-4-1, 3-2-3, 3-3-1, 3-2-1, and 1-3-1).

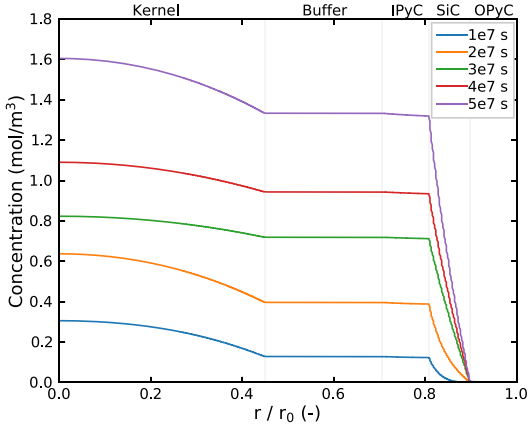

Fig. 25. Concentration of silver in AGR-1 compact 6-1-1 over time. The abrupt drop in concentration is due to the low diffusivity of silver in SiC.

Two analyses were run for each compact with failed particles. The first was the standard analysis already described. In the second, which targeted failed particles, the fission product diffusivity of the SiC layer was set to a large value (10^{-6} m^2/s [3]). The release fraction becomes:

$$f_{net} = \frac{f_i(n - n_f) + f_f n_f}{n} \tag{23}$$

where f_{net} is the overall release fraction, f_i is the release fraction from the intact particle, f_f is the release fraction from the failed particle, n is the total number of particles in the compact, and n_f is the number of failed particles in the compact.

First, consider Fig. 26, which shows, for Compact 6-1-1, the concentrations of silver, cesium, and strontium at 5×10^7 s (approximately 580 days). The data for silver is the same as in Fig. 25. The concentrations of cesium and strontium are significantly higher than for silver. It is also worth noting that the concentration of strontium across the particle is qualitatively different than the concentration of cesium (and of silver, as seen in Fig. 25). Whereas the other two fission product concentrations drop dramatically at the SiC layer, the concentration of strontium drops dramatically at the interface between the kernel and the buffer. This is due to a very low diffusion coefficient for strontium in the kernel. Little strontium is released from the kernel.

The results for cesium release with intact particles are found in Fig. 27, and results for cesium release with failed particles are in

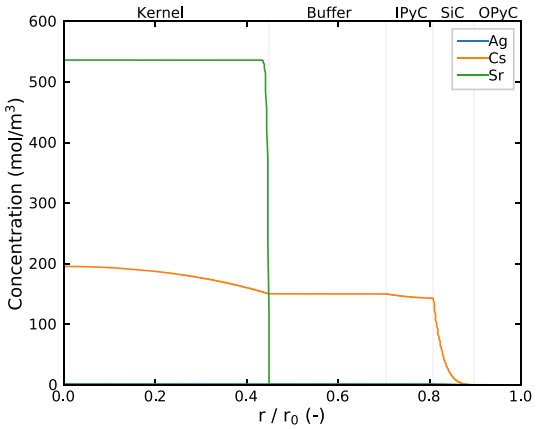

Fig. 26. Concentration of silver, cesium, and strontium in Compact 6-1-1 at 5×10^7 s. The concentration of silver is better seen in Fig. 25.

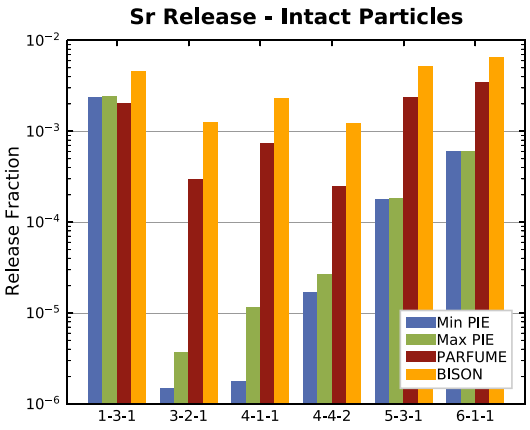

Fig. 28. Comparison of measured and computed cesium release fractions for three compacts with one or two failed particles.

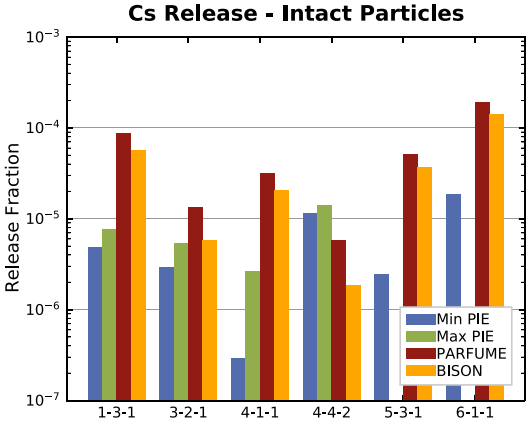

Fig. 27. Comparison of measured and computed cesium release fractions for six compacts with no failed particles.

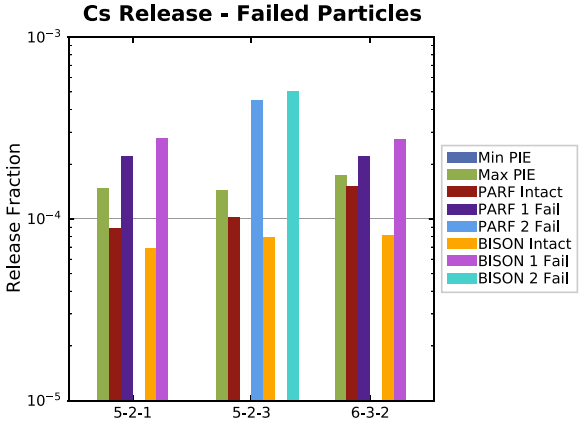

Fig. 29. Comparison of measured and computed strontium release fractions for six compacts with no failed particles.

Fig. 28. Aside from Compact 4-4-2, both PARFUME and BISON compute a higher release than seen in PIE for compacts with no failed particles (although for Compact 3-2-1, BISON's prediction nearly matches the maximum PIE value). Both PARFUME and BISON compute a higher release than seen in PIE for compacts with failed particles. Compared to PARFUME, BISON predicts a slightly lower release for cesium with intact particles and a slightly higher release for cesium with failed particles.

The results for strontium release with intact particles are in Fig. 29, and results for strontium release with failed particles are in Fig. 30. For compacts with intact particles, the PARFUME and BISON results are fairly consistent from compact to compact, while the PIE results show a large variation. These results show room for improvement, perhaps in the values of the diffusion coefficients. For compacts with failed particles, both PARFUME and BISON compute a higher release than seen in PIE. Compared to PARFUME, BISON predicts a slightly higher release for strontium, both with intact particles and with failed particles. In the case of strontium, it is interesting to note that predictions change only very slightly with the inclusion of failed particles. This is due to most of the strontium being held in the fuel kernel, never migrating outward to where a failed SiC layer would affect its release.

Differences in cesium and strontium diffusion between intact and failed particles can be seen in Fig. 31. This figure shows concentrations in Compact 6-3-2 at 5×10^7 s (approximately 580 days) for an intact particle and one in which the diffusion coefficient of the SiC layer was set to 10^{-6} m^2/s. For cesium in the intact case, the concentration drops dramatically across the SiC layer, as previously shown. For cesium in the case of a failed particle, the concentration hardly drops across the SiC layer (the dashed line is horizontal across the SiC layer). However, for strontium, the intact and failed results are indistinguishable. Small differences do exist but are not visible at this scale. The reason for this is that the kernel retains nearly all the strontium. The higher diffusion coefficient in the SiC layer has very little effect. Again, this effect is manifest in Fig. 30.

For silver, cesium, and strontium diffusion in AGR-1, BISON's computed results compare reasonably well to PIE values and values computed by PARFUME. BISON's results were computed using diffusion coefficients in [10]. Other researchers have calibrated diffusion models to match AGR-1 data [19], but this has not been done here. Considering the four compacts with known lower and upper bounds on release (based on PIE) in Fig. 27, BISON's results are at or above the upper bound in three of the cases and below the lower bound in the other. Thus, it will likely be difficult to find diffusion model coefficients that accurately compute release fractions for all compacts. Subtleties, such as temperature variations within a compact, may play an important role and need to be included for more accurate validation of AGR-1 fission product release fraction calculations. The exploration of calibrated coefficients and compact-level temperature variations has been left as future work.

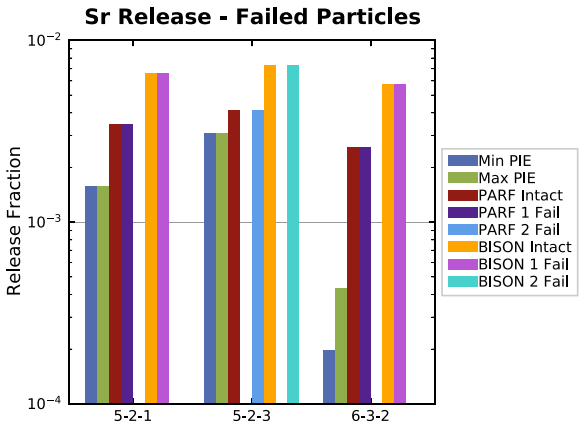

Fig. 30. Comparison of measured and computed strontium release fractions for three compacts with one or two failed particles.

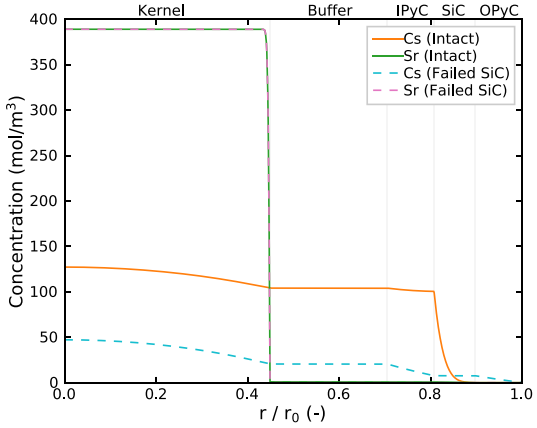

Fig. 31. Concentrations of cesium and strontium for an intact and a failed particle in Compact 6-3-2.

6. Conclusions

Significant advances in BISON's capabilities to model TRISO fuel have recently been made. BISON is able to build a one-dimensional or two-dimensional TRISO mesh automatically. This dramatically speeds up analysis and enables automated sensitivity and parameter exploration studies.

Many new material models are available for the fuel kernel, buffer, pyrolytic carbon, and SiC. These models include mechanical (elastic, creep, irradiation strain), thermal (thermal conductivity, specific heat), mass diffusion, and fission gas production and release models.

A significant effort has been made to ensure that solutions computed by BISON are correct. A rigorous verification exercise was completed in which BISON was shown to converge to the correct analytic solution upon mesh refinement for a set of nontrivial problems. Ten benchmark cases for fuel performance from the IAEA CRP-6, originally run with BISON several years ago, were rerun. The remaining three cases were run for the first time. In addition, the diffusion cases from CRP-6 were run for the first time. In all cases, results either matched analytic solutions or, where no analytic solution exists, were comparable to results computed from other codes.

BISON results have been validated against experimentally obtained fission product diffusion data. The AGR-1 experiment, in which a number of capsules loaded with TRISO particles were irradiated and fission product diffusion measured, provides data on the movement of silver, cesium, and strontium. For all three species, the BISON results compare favorably with the experimental data and with results computed by PARFUME.

The understanding of fission product diffusion requires significant investigation, in no small part due to the fact that diffusion is often not the mechanism by which fission products transverse a fuel particle. In many cases, movement is accelerated by chemical changes, grain boundaries, or cracks. These phenomena are not understood well and are not modeled at present. Instead, these phenomena are lumped together with Fickian diffusion, resulting in the determination and use of effective diffusion parameters. Properly modeling these mechanisms will require close coordination with lower-length-scale researchers. Another area that needs further development is improving the new statistical failure capability in BISON by adding support for more failure modes, such as a chemical attack on the SiC layer. Finally, more validation work is needed. In particular, the Advanced Gas Reactor (AGR) test series includes much more data, and BISON's ability to predict the response of TRISO fuel will be checked against that data.

Declaration of Competing Interest

The authors declare that they have no known competing financial interests or personal relationships that could have appeared to influence the work reported in this paper.

Acknowledgments

The partnership of Kairos Power, LLC, including contributions to the source code and documentation for TRISO capabilities, is gratefully acknowledged.

This work was funded by the DOE's Nuclear Energy Advanced Modeling and Simulation (NEAMS) and Consortium for Advanced Simulation of Light Water Reactors (CASL) programs. The submitted manuscript has been authored by a contractor of the U.S. Government under Contract DE-AC07-05ID14517. Accordingly, the U.S. Government retains a non-exclusive, royalty-free license to publish or reproduce the published form of this contribution, or allow others to do so, for U.S. Government purposes.

References

[1] J.D. Hales, R.L. Williamson, S.R. Novascone, D.M. Perez, B.W. Spencer, G. Pastore, Multidimensional multiphysics simulation of TRISO particle fuel, J. Nucl. Mater. 443 (2013) 531–543, doi:10.1016/j.jnucmat.2013.07.070.
[2] International Atomic Energy Agency, Advances in High Temperature Gas Cooled Reactor Fuel Technology, Technical Report IAEA-TECDOC-1674, 2012.
[3] B.P. Collin, D.A. Petti, P.A. Demkowicz, J.T. Maki, Comparison of silver, cesium, and strontium release predictions using PARFUME with results from the AGR-1 irradiation experiment, J. Nucl. Mater. 466 (2015) 426–442, doi:10.1016/j.jnucmat.2015.08.033.
[4] G.K. Miller, D.A. Petti, J.T. Maki, D.L. Knudsen, W.F. Skerjanc, PARFUME Theory and Model Basis Report, Technical Report INL/EXT-08-14497, Idaho National Laboratory, 2009.
[5] Computational Mechanics and Materials Department, Idaho National Laboratory, BISON: a finite element-based nuclear fuel performance code, 2020, (http://mooseframework.org/bison).
[6] Dassault Systèmes, Abaqus unified FEA, 2020, (https://www.3ds.com/products-services/simulia/products/abaqus/).
[7] D. Petti, P. Martin, M. Phelip, R. Ballinger, Development of Improved Models and Designs for Coated-Particle Gas Reactor Fuels, Technical Report INL/EXT-05-02615, Idaho National Engineering and Environmental Laboratory, 2004.
[8] W. Jiang, J.D. Hales, B.W. Spencer, B.P. Collin, A.E. Slaughter, S.R. Novascone, A. Toptan, K.A. Gamble, R. Gardner, TRISO particle fuel performance and failure analysis with BISON, J. Nucl. Mater. (2021) 152795, doi:10.1016/j.jnucmat.2021.152795.
[9] Sandia National Laboratories, CUBIT: Geometry and mesh generation toolkit, 2020, (http://cubit.sandia.gov).
[10] International Atomic Energy Agency, Fuel Performance and Fission Product Behavior in Gas Cooled Reactors, Technical Report IAEA-TECDOC-978, 1997.
[11] P.J. Roache, Verification and Validation in Computational Science and Engineering, Hermosa Publishing, Albuquerque, NM, 1998.

[12] K. Salari, P. Knupp, Code Verification by the Method of Manufactured Solutions, Technical Report SAND2000-1444, Sandia National Laboratories, 2000, doi:10.2172/759450.
[13] W.L. Oberkampf, C.J. Roy, Verification and Validation in Scientific Computing, first ed., Cambridge University Press, Cambridge, UK, 2010.
[14] M.P. McHale, et al., Standard for Verification and Validation in Computational Fluid Dynamics and Heat Transfer, Standard ASME V&V 20-2009, American Society of Mechanical Engineers, 2009.
[15] A. Toptan, N.W. Porter, J.D. Hales, R.L. Williamson, M. Pilch, FY20 Verification of BISON Using Analytic and Manufactured Solutions, Technical Report CASL-U-2020-1939-000; SAND2020-3887R, CASL, 2020, doi:10.2172/1614683.
[16] A. Toptan, N.W. Porter, J.D. Hales, B.W. Spencer, M. Pilch, R.L. Williamson, Construction of a code verification matrix for heat conduction with finite element code applications, Journal of Verification, Validationand Uncertainty Quantification 5 (4) (2020), doi:10.1115/1.4049037. 041002
[17] J.H. VanSant, Conduction Heat Transfer Solutions, Technical Report UCRL 52863-Rev.l; DE87 012387, Lawrence Livermore National Lab., 1983, doi:10.2172/6224569.
[18] R.B. Bird, W.E. Stewart, E.N. Lightfoot, Transport Phenomena, John Wiley & Sons, Inc., New York, New York, 1960.
[19] D. Schappel, K. Terrani, L. Snead, B. Wirth, Modeling radionuclide release of TRISO bearing fuel compacts during post-irradiation annealing tests, Nuc. Eng. Des. 357 (2020) 110428, doi:10.1016/j.nucengdes.2019.110428.